Characterization of the dynamics of block copolymer microdomains with local morphological measures

S. Rehse,[1,*] K. Mecke,[2] and R. Magerle[1]
[1]*Chemische Physik, Technische Universität Chemnitz, Reichenhainer Straße 70, D-09126 Chemnitz, Germany*
[2]*Institut für Theoretische Physik, Universität Erlangen-Nürnberg, Staudtstraße 7, 91058 Erlangen, Germany*
(Received 9 November 2007; revised manuscript received 15 February 2008; published 23 May 2008)

We investigate the structure formation in thin films of cylinder forming block copolymers. With *in situ* scanning probe microscopy image sequences can be recorded with high temporal (2 min per frame) and spatial (10 nm) resolution. We compare different image processing methods for quantitative analysis of the large amount of data. Computing local Minkowski functionals yields local geometrical and morphological information about the observed structures and enables us to track their evolution with time. An alternative characterization method is to reduce the gray scale images to their skeleton and to classify and count the branching points of the skeletonized structure. We tracked the temporal evolution of these measures and computed correlation functions.

DOI: 10.1103/PhysRevE.77.051805 PACS number(s): 82.35.Jk, 02.40.−k, 05.40.−a

I. INTRODUCTION

Within the last decade, block copolymers have become more and more interesting for nanotechnological applications, such as patterned media storage, nanostructured membranes, or photonic crystals [1]. For these applications, which need highly ordered areas of nanometer scaled structures, thin films of block copolymers are of particular interest since they offer a rather straightforward way to align the microdomain structure parallel to the film plane. Various methods such as, for example, graphoepitaxy [2], electric fields [3–5], and shear alignment [6] have been demonstrated for aligning microdomains parallel and perpendicular to the film plane. While the formation of equilibrium structures in these films was already intensively studied [7–12], the elementary processes of pattern ordering and microdomain dynamics, such as motion of individual structural defects [13–19], form fluctuations of microdomains, or orientational reordering [14,16] are still subject to research. While tracking the evolution of individual defects [17–19], fast and repetitive transitions between distinct defect configurations can be observed [18]. Tsarkova *et al.* postulated that the dynamics of neighboring defects might be correlated [18]. Another interesting topic is the study of elementary processes during the rearrangement of block copolymer microdomains upon the change of an external control parameter by applying, e.g., electric fields [20–28], shear flow [29–33], or temperature changes [34,35].

With scanning probe microscopy (SPM) [36,37] it is possible to study the occurring structures with high spatial resolution in real space. Here, SPM *in situ* measurements of melts [18,19] and concentrated solutions of block copolymers [17] during annealing are an important advance compared to the method of stepwise annealing and subsequent SPM measurements which was used in previous works [13–16]. Measuring *in situ* allows us to record snapshot images of the sample surface with a rate of up to 1 frame per minute. With modern high speed SPMs data-acquisition times reaching video rates can be achieved, enabling the study of a wide variety of dynamical processes with unprecedented temporal resolution (for a review, see Ref. [38]). Besides experimental studies, also detailed theoretical simulations of the microdomain dynamics and the involved elementary processes have been made [17,23,25,26,28,31–33,39,40].

To compare theory and experiment it is necessary to describe the experimentally measured data and the simulated data in a quantitative way. Many authors [13,14,17–19] classify and count defects manually. The drawback of this method is that it is subjective and that it takes a lot of time. Hence, it is only applicable to few, small data sets. For an adequate statistical analysis of large data sets capturing the structure forming processes we have recently introduced an automated method for classification and counting defects [41].

Harrison *et al.* examined the coarsening dynamics of a single layer of cylinder forming block copolymer microdomains by SPM measurements [14,16]. They have computed the microdomain or stripe orientation by measuring the local intensity gradient field $\Theta(\vec{r})$ of the SPM images. On the basis of this information they have calculated local orientational and translational order parameters. Doing so for different annealing times they have extracted time-dependent orientational correlation lengths which grow with the average spacing between $\pm\frac{1}{2}$ disclinations. Furthermore, they have detected disclinations automatically by computing closed path integrals of the variation of $\Theta(r)$. Following the density of disclinations and comparing it with the evolution of the orientational correlation length they have suggested a dependence of the dynamics of the orientational correlation length on the interaction of topological defects. By tracking the evolution of several disclinations, they also observed dominant mechanisms of disclination annihilation.

Besides the investigation of cylinder forming block copolymers also sphere forming block copolymers have been investigated [42–44]. Here, disordered hexagonal point pat-

*Author to whom correspondence should be addressed; sabine.scherdel@physik.tu-chemnitz.de

terns are studied by computing a Fourier transformation of the SPM images and Voronoi diagrams (and Delaunay triangulation, respectively) of the sphere centers. Disclinations are found by counting pairs of irregular shaped Voronoi cells (or sphere centers with an unusual number of neighbors, respectively). From the Voronoi diagrams (and Delaunay triangulation, respectively) also orientational and translational order parameters were calculated and followed during annealing.

Soille [45] has used morphological operators, such as opening and closing, to compute the orientation field of the striped pattern of a cylinder forming block copolymer. By applying the watershed transformation to an SPM image of a block copolymer film with increasing film thickness different morphological structures have been separated. Soille has also computed the local connectivity number of an SPM image containing three different types of microdomains and has showed that this measure is also useful to discriminate different morphologies.

Another approach to analyze phase separating block copolymer systems is to use topological and geometrical quantities, such as Minkowski functionals [46–48]. These measures are well known in image analysis [49], mathematical morphology [50], and integral geometry [52,53]. They are numerically robust, independent of statistical assumptions on the distribution of phases, and can be calculated effectively from binary images [52–54]. They provide information on connectivity, shape, and content of spatial morphologies. As Minkowski functionals are calculated for binary (i.e., black and white) images it is important to decide which pixels are in or outside the pattern. One approach is to compute the Minkowski values for a set of thresholds [54]. In this way, threshold-dependent curves are obtained which depend on the gray scale distribution of the initial images. Comprising physical knowledge this information can be further reduced [46,53] and used for a quantitative comparison of experimental and simulation data [55,56].

Also many other—measured as well as simulated—complex patterns can be characterized with Minkowski functionals in two dimensions as well as in three dimensions [53,54,57–60]. Minkowski functionals have been also used to study structure formation in thin films of polymer blends [61–67]. However, in all of these applications only the complete images have been analyzed. As small fluctuations around individual defects contribute only little to these large integration areas, these fluctuations are not captured by this kind of Minkowski analysis.

Our approach is to analyze time series of block copolymer structure formation with local Minkowski measures which are calculated for small areas centered at each pixel of a binarized SPM image. Hereby, we concentrated on the local Euler characteristic which is in particular sensitive to topological changes of the pattern. Alternatively, we have reduced the gray scale structures to their skeleton and classified the obtained graphs by marking end and branching points similar to the method described in Ref. [41]. Subsequently, we counted the different types of defects and followed their evolution with time. In the resulting curves transitions between different morphologies are clearly visible. Besides these larger changes also smaller fluctuations exist.

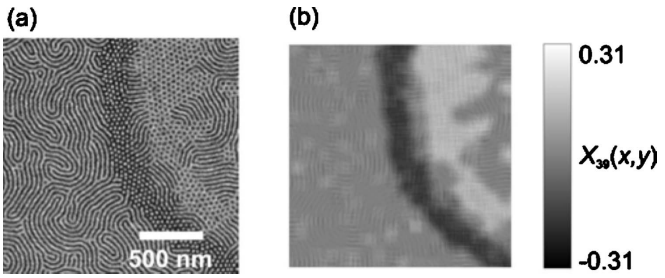

FIG. 1. (a) Tapping mode SPM phase image $P(x,y)$ of a thin film of a cylinder forming polystyrene-*block*-polybutadiene-*block*-polystyrene triblock copolymer (data set A). Bright corresponds to polystyrene microdomains. Depending on the film thickness the block copolymer shows different structures, such as parallel cylinders (bright stripes), upright standing cylinders (bright dots), or perforated lamellae (dark dots). Here, the film thickness decreases from left to right. (b) Map of the local Euler characteristic $X_{39}(x,y)$ of (a) calculated with box size 14×14 pixels and threshold $\rho=0.39$. It can be used as a morphology map mapping different structures to different gray values. All quantities are dimensionless.

Therefore, we have analyzed the temporal evolution of Minkowski measures and the number of branching points and compared the results with the time constants obtained by calculating laterally averaged pixel-to-pixel correlations. The methods demonstrated in this paper are applicable to a large group of different SPM experiments and simulations on the block copolymer microdomain dynamics.

II. METHODS

A. Experimental data sets

We demonstrate our image analysis methods on two data sets of thin films of cylinder forming block copolymers. The first data set (data set A) is a tapping mode SPM phase image [Fig. 1(a)] of a thin film of a cylinder forming polystyrene-*block*-polybutadiene-*block*-polystyrene triblock copolymer (SBS) with a film thickness corresponding to one and two layers of cylinders. The image is from the data set presented in Ref. [69], where experimental details are given. Figure 1 shows a similar structure as the sample shown in Fig. 6(b) of Ref. [69].

The second one (data set B) is a series of tapping mode SPM phase images of a thin film of a cylinder forming polystyrene-*block*-polybutadiene (SB) copolymer. It shows the changes of the microdomain structure during annealing in solvent vapor. The data set is from Ref. [68]. The SB block copolymer was obtained from Polymer Source Inc. with molecular weights of blocks $M_{w,\mathrm{PS}}=13.6$ kg/mol and $M_{w,\mathrm{PB}}=13.7$ kg/mol and a polydispersity of $M_w/M_n=1.03$. A thin film was prepared on a mica substrate by spin coating from a toluene solution to yield a uniform thickness of approximately 50 nm. The samples were first annealed for approximately 2.5 h in a chloroform vapor which was increased stepwise from 0% to 70% of saturated chloroform vapor. Details of the experimental setup and procedures are described in Refs. [11,17,69]. The thin film phase behavior of the SB diblock copolymer is similar as that of the SBS

triblock copolymer studied in Refs. [11,17,69]. The series of SPM images was measured *in situ* in a liquid cell (Veeco Instruments Inc.) with the specimen swollen in a chloroform vapor. During the measurement the relative chloroform vapor pressure was increased stepwise from 10% to 80% of saturated chloroform vapor. Starting from 10% of saturated chloroform vapor, the vapor pressure was increased to 20%, 30%, 40%, 50%, 60%, 70%, 75%, and 80% at frames 6, 11, 18, 31, 61, 89, 138, and 153, respectively. During the increase of solvent vapor the film thickness increases which causes structural transformations. The resulting series of SPM images are 16 bit gray scale images (256×256 pixel) with a size of $1\ \mu\text{m} \times 1\ \mu\text{m}$. The temporal resolution is 2 min per frame.

B. Image preprocessing

The gray scale of SPM phase images depends on several operating parameters of the instrument which often change during the measurement. Image preprocessing is necessary to correct for this. To get rid of the tilt of the sample relative to the scan level we fitted a plane to the image and subtracted it from the image values. Furthermore, using the image analysis software of the SPM [70] we fitted a line to each row of pixels in the image and subtracted it from the respective row. After these steps the gray scale histogram of each image was equalized with the Matlab (The MathWorks Inc.) routine histadapt and normalized to the range 0 to 1. In a final step the images were registered as described in Ref. [71].

C. Minkowski functionals

Minkowski functionals are morphological measures well known in digital picture analysis [49], mathematical morphology [50], and integral geometry [51] which allow one to characterize binary (black and white) images. Morphological measures are defined as continuous and motion invariant functionals which are additive, e.g., $W(A \cup B) = W(A) + W(B) - W(A \cap B)$, where A, B are sets in the Euclidean space. For details, see Refs. [52,53]. The theorem of Hadwiger [72] states that all morphological measures are a linear combination of Minkowski functionals.

In two-dimensional space which we consider in our SPM images the Minkowski functionals are related to three familiar geometrical measures: The white area fraction A, the length of the boundary line between black and white regions P, and the Euler characteristic X which describes the topology of the white structure, i.e., the connectivity of the black and white regions.

The area fraction A is computed by counting all white pixels in the image. It is normalized by dividing it through the total number of pixels N. The perimeter P is computed as the number of pairs of neighbored black and white pixels and it is also normalized by N. The Euler characteristic is the difference of the number of black and white components normalized by N. A black or white component is defined as a region of connected black or white pixels, respectively.

Because of the additivity of the Minkowski functionals they can be calculated in small vicinities of 2×2 pixels. For pixels of equal side length, the local Minkowski functionals are rotationally invariant. So, with only six different constellations of pixels the Minkowski functionals of the whole image can be computed in a fast way by using a lookup table [56].

As the SPM measurements yield 16 bit gray scale images the data must first be reduced to binary images. However, in the binarization process a lot of information is lost. Hence, we have computed the Minkowski values for a set of threshold values reaching from 0 to 1 within equidistant intervals of 0.01 [54]. In this paper, we calculate the Minkowski functionals not for the complete image but for small regions of size $m \times m$. In this way we obtain measures which reveal information of the local morphology for every pixel of the binarized SPM image except for boundary pixels.

D. Skeletonization

Another approach to characterize block copolymer microdomain structures is to skeletonize the binarized images. This can be done with different algorithms (for an overview see, e.g., Refs. [73,74]). We have used the skeletonization method implemented in ImageJ (Wayne Rasband, National Institute of Health, USA). Due to noise in the SPM images artifacts of the skeleton exist. They are, e.g., short protrusions or clusters of threefold branching points at positions where cylinders branch. These artifacts are identified and removed as described in Ref. [41].

We interpreted the resulting skeleton as a graph which we characterized by its junctions and the number of edges originating from each junction. In this way, a junction with one neighbor (end point) was assigned the value 1, a junction with two neighbors (line point) was assigned the value 2, and so on. For every frame we counted how many junctions of each value are in the image. Doing so for all frames allowed us to observe how the number of junctions with different value was changing with time.

III. RESULTS AND DISCUSSION

A. Minkowski functionals

Figure 1(a) shows a typical SPM image of a thin film of block copolymer containing different microdomain structures such as parallel cylinders ($C_{\parallel}$), upright standing cylinders ($C_{\perp}$), and perforated lamellae (PL). We binarized the normalized gray scale image with the threshold $\rho = 0.39$ and computed the local Euler characteristic X_{39} with local box sizes of 14×14 pixels. As it can be seen in Fig. 1(b) the different morphological regions in Fig. 1(a) are assigned different X_{39} values yielding a new gray scale image which can be considered as a morphology map of the original SPM image [75]. Here, the box size $m = 14$ equals approximately 2 times the cylinder-cylinder distance. With increasing box size this morphology map gets more and more blurred. By averaging over larger integration areas large morphological features are more emphasized in the morphology map whereas smaller features are disappearing. Decreasing the box size, in contrast, causes that more and more details of the morphological information are visible. The smaller the integration area is, the more artifacts appear in the morphology

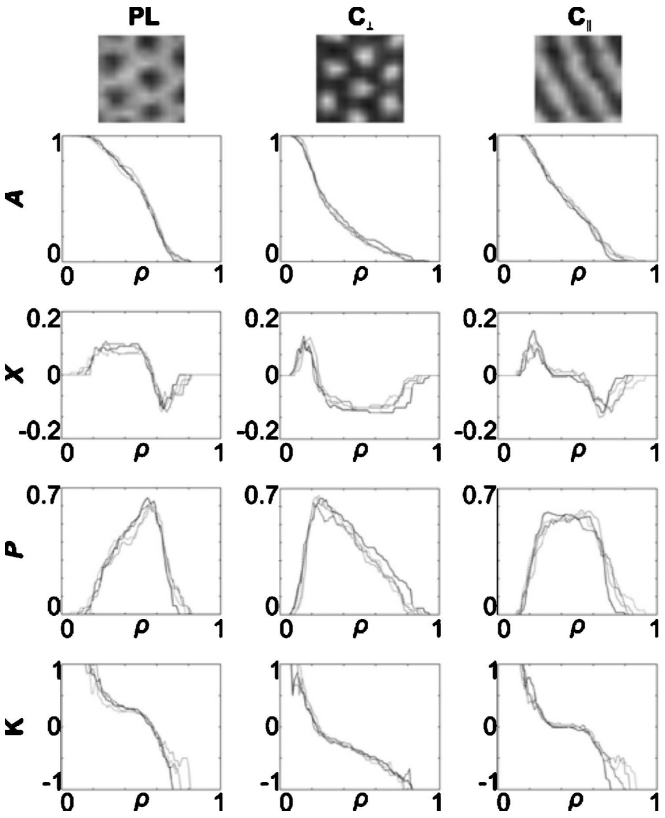

FIG. 2. Area A, Euler characteristic X, perimeter P, and the ratio X/P as functions of the threshold ρ calculated for different samples with different morphologies using a box size of 14×14 pixels. The first row shows examples of the different types of microdomain structure. In each diagram four curves are shown which correspond to four different samples of the same type of structure. All quantities are dimensionless.

map. Therefore, m must be chosen carefully depending on the kind of information which should be extracted.

To examine if there are thresholds where different morphologies can be discriminated in a robust way we plotted the threshold dependent Minkowski measures A_ρ, P_ρ, and X_ρ for different morphologies at several randomly chosen spots of the SPM image. Obviously, the values of the Minkowski functionals depend strongly on the chosen threshold. For $\rho=0$ and $\rho=1$, e.g., the binarized image is uniform and, therefore, no discrimination between the different gray scale morphologies is possible. However, Fig. 2 shows that the shape of the curves is characteristic for the respective kind of pattern (top of Fig. 2). As an example, we will discuss the Euler characteristic X_ρ for the three different morphologies. For perforated lamellae the curve starts at zero and increases then to a plateau with a positive X_ρ value. At $\rho\approx0.5$ the curve decreases very steep to a negative X_ρ value at $\rho\approx0.7$. Finally, X_ρ increases to zero for $\rho>0.9$. In the case of upright standing cylinders the Minkowski curve appears mirrored compared to that of the PL morphology. It starts at zero but then increases first to a small positive peak and decreases at $\rho\approx0.2$ to a plateau with negative X_ρ value. This is due to the fact that there are bright dots in SPM images of the $C_\perp$ morphology and dark dots in case of the PL morphology. Therefore, the image of a $C_\perp$ morphology is the inverse image of a PL morphology and vice versa. The threshold dependent Euler characteristic of parallel cylinders ($C_\parallel$), however, has two distinct peaks (a positive peak at $\rho\approx0.2$ and a negative peak at $\rho\approx0.7$) separated by a plateau between $\rho\approx0.3$ and $\rho\approx0.6$ with $X_\rho=0$. Since in all of these curves a plateau exists within the interval from $\rho\approx0.3$ to $\rho\approx0.5$, a single threshold $\rho^*\in[0.3,0.5]$ could be chosen for which the Minkowski measures are rather independent of small differences in the normalization of gray values. We calculated the Minkowski measures for cylinder-cylinder distances of approximately 7 pixels. The threshold dependence of Minkowski measures is similar for images with cylinder-cylinder distances of 35 pixels.

A further improvement of the robustness can be achieved by calculating the ratio $K_\rho=X_\rho/P_\rho$ (bottom line of Fig. 2) which corresponds to the mean curvature of the border line between black and white regions. As can be seen in Fig. 2, the fluctuations of this ratio are noticeably smaller than those of X_ρ and P_ρ. Moreover, the form of the threshold depending curve is very intuitive. For small (large) threshold values ρ many isolated small regions (holes) exist with a high mean curvature of the corresponding boundary lines. In the interval $\rho\in[0.3,0.5]$ K_ρ reflects the morphology of the investigated pattern in a robust way. It has a positive value for the PL morphology, a negative value for the $C_\perp$ morphology, and equals 0 for the lamellar morphology. K_ρ is a robust and intuitively understandable measure for characterizing with only one parameter the different structures occurring during block copolymer microdomain transitions.

The possibility to distinguish between different morphologies by the form of the Minkowski curves encouraged us to investigate phase transitions occurring in our experiments by local Minkowski measures. We chose two areas from a sequence of larger SPM images (Fig. 3). The first area [Fig. 4(a)] depicts a spot where the morphology clearly changes with time from $C_\parallel$ to partly PL and finally to mainly $C_\perp$. In contrast, in Fig. 4(b) the morphology is $C_\parallel$ and does not change significantly during the observation period. The size of the samples (40×40 pixel) is approximately 4 times the cylinder-cylinder distance.

For these two areas we computed the Euler characteristic for all time steps and thresholds. In Fig. 5 the value of X_ρ is displayed as gray value as a function of time step n and threshold ρ. Following the evolution of the threshold dependent Euler characteristic X_ρ with time in Fig. 5(a) a change of the curve shape can clearly be seen at $n\approx120$ (see gray arrow). This change occurs at the same time at which a morphology change can be seen in the individual images. In contrast, in Fig. 5(b), where no morphology change is visible in the SPM images the shape of the curve is essentially the same for all time steps.

Although the general shape of the Euler characteristic X_ρ is similar for similar morphologies slight fluctuations exist in Fig. 5. To examine this we chose one constant threshold $\rho_1=0.39$ at which the transition between the different shaped Euler characteristic curves is pronounced. For this threshold we plotted the Euler characteristic X_{39} over time (Fig. 6). The X_{39} curve in Fig. 6(a) which corresponds to the area shown in Fig. 4(a) first fluctuates around a constant mean value and

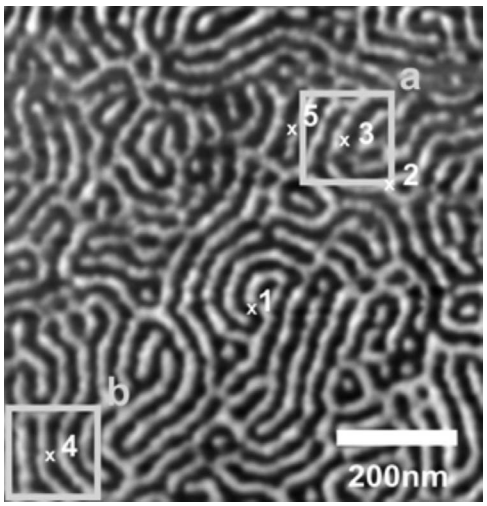

FIG. 3. Tapping mode SPM phase image of a polystyrene-block-polybutadiene diblock copolymer (image size 213×221) swollen in chloroform vapor (data set B). The image is the first of a sequence of images displaying the microdomain dynamics during further annealing. The temporal evolution of region (a) and (b) is shown in Fig. 4. Crosses and numbers indicate the position of samples that are analyzed in Figs. 7 and 8.

decreases after approximately 120 time steps. This indicates a morphology transition from a parallel cylinder structure to a dotlike defect structure. The X_{39} curve in Fig. 6(b) which corresponds to the data set shown in Fig. 4(b) fluctuates around a mean value that stays nearly constant for all time steps. Thresholding X_ρ at a different threshold value $\rho_2 = 0.33$ yields curves X_{33} which have a similar shape but differ in the form of the fluctuations.

We now have analyzed these curves by computing temporal correlation functions of the data sets marked in Fig. 3. For sample 1, 4, and 5 the correlation curves are decreasing very fast within $\tau < 3$ and remain constant for larger τ, where τ is the time lag in units of frame numbers [Fig. 7(a)]. No characteristic time constants can be recognized. The correlation curves of samples 2 and 3 decrease slowly with a time

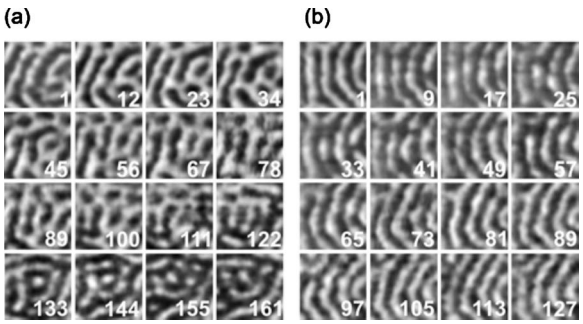

FIG. 4. Two samples (40×40 pixel) of the film shown in Fig. 3 observed during increasing saturation with chloroform vapor from 10% to 80%. The individual images show the dynamics of the film. The frame rate is about 2 min per frame. The numbers indicate the frame numbers. (a) Position (a) of Fig. 3. The whole data set consists of 161 images. (b) Position (b) of Fig. 3. The whole data set consists of 127 images.

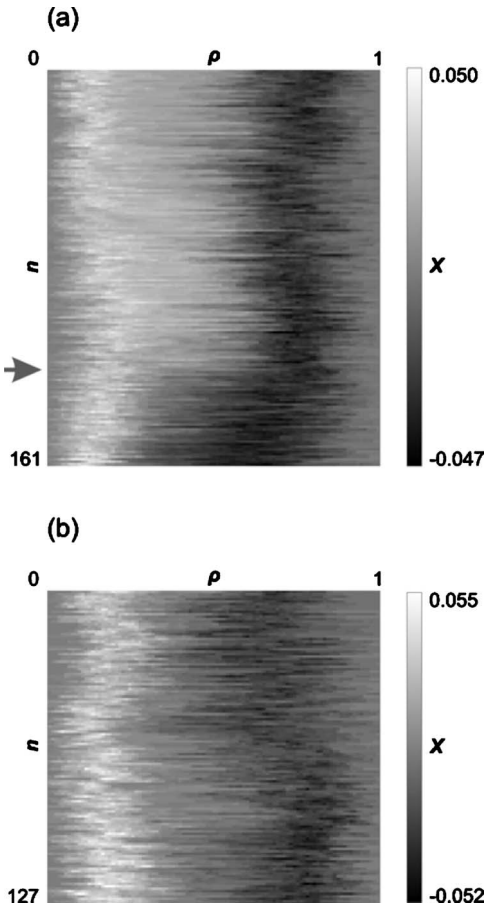

FIG. 5. Gray scale maps of the Euler characteristic X at box size 40×40 as a function of density threshold ρ and frame number n: (a) of the sample shown in Fig. 4(a), (b) of the sample shown in Fig. 4(b). All quantities are dimensionless.

constant of about 40–50 frames. To test if these time constants reflect only the occurring morphology transition as indicated by the decrease of X_{39} and X_{33} for $n > 100$ [Fig. 6(a)] we restricted the analysis of the time-dependent Euler

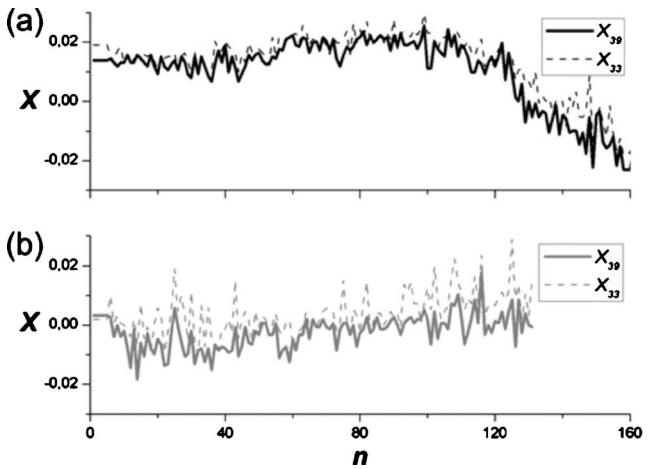

FIG. 6. Euler characteristic $X_{39}(n)$ and $X_{33}(n)$ for density threshold $\rho = 39$ and $\rho = 33$, respectively, versus frame number n: (a) corresponds to the sample shown in Fig. 4(a), (b) corresponds to the sample shown in Fig. 4(b). All quantities are dimensionless.

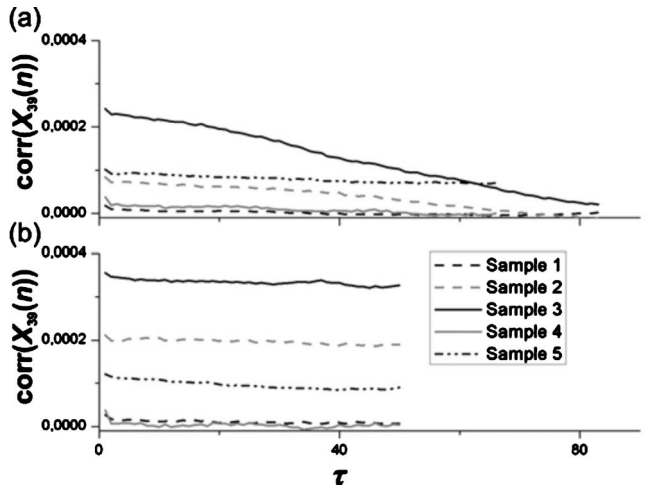

FIG. 7. Correlation function of the Euler characteristic $X_{39}(n)$ versus time lag τ. The five curves correspond to different samples of Fig. 3, where sample 3 corresponds to Fig. 4(a) and sample 4 corresponds to Fig. 4(b). (a) Correlation functions calculated in the intervals [1,161] and [1,127], (b) correlation functions calculated in the interval [1,100]. All quantities are dimensionless.

characteristics to the interval $n \in [1,100]$ in which the time series of X_{39} are approximately constant. Figure 7(b) shows that for this smaller time interval the correlation functions are constant for $\tau > 3$ for all five samples. This shows that no temporal correlations can be detected. The value of the correlation functions normalized by the squared mean value of the time series is a measure of the amplitude of the temporal fluctuations.

We compared these curves with the laterally averaged pixel-to-pixel correlation functions (Fig. 8). For this, we followed for every pixel position in the boxes indicated in Fig. 3 the evolution of the respective gray value with time and computed the correlation function of these curves. Then we

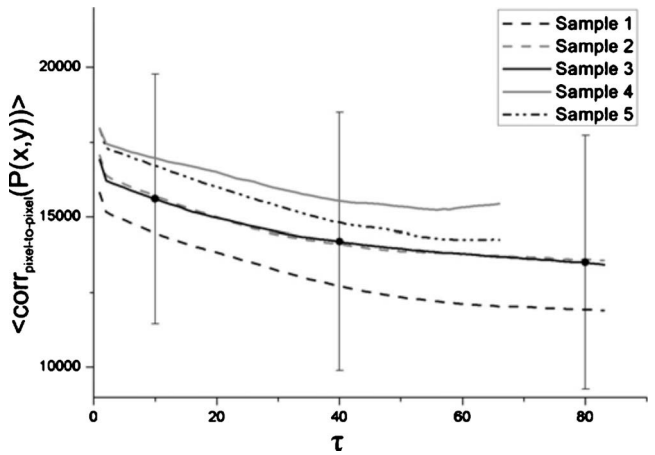

FIG. 8. Averaged pixel-to-pixel correlations of image samples $P(x,y)$ (where x and y are the spatial coordinates) versus time lag τ. The curves correspond to the same samples as in Fig. 7. At three spots error bars indicating the standard deviation of the correlation function corresponding to sample 3 are shown. The standard deviation is similar for all τ and for all samples. All quantities are dimensionless.

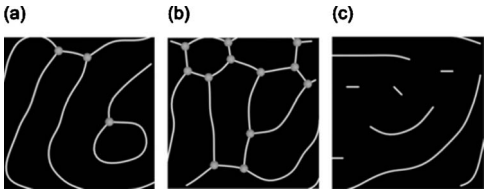

FIG. 9. Reduced skeleton of frame 1, 67, and 161 of the sequence of images shown in Fig. 4(a).

averaged all 40×40 correlation curves. The resulting averaged correlation curves show a decrease with time constants of about 20–30 frames. Furthermore, the shape of the pixel-to-pixel correlation function does not differ significantly for the different types of morphologies. The rather large standard deviation does not allow for a more detailed comparison. However, correlation functions are known to be insensitive to shape. For instance, in Ref. [76] one may find for point patterns a discussion of which spatial features are visible in correlation functions and also a comparison of correlation functions with the shape-sensitive Minkowski functionals.

B. Skeletonization

By skeletonizing and classifying the SPM images shown in Fig. 4(a) we yield a time series of two-dimensional graphs consisting of white lines and classified branching (Fig. 9). Figure 9(a) shows the graph corresponding to frame 1 in Fig. 4(a), Fig. 9(b) corresponds to frame 70 [not shown in Fig. 4(a)] and Fig. 9(c) corresponds to the last frame in Fig. 4(a). The details of the resulting graph depend on the binarization method and on the image preprocessing. To get a better comparison with the Minkowski method we also binarized the SPM images with a fixed threshold $\rho = 0.39$.

Figure 10(a) shows the temporal evolution of the number of threefold branchings (y connections) for samples 3 and 4 in Fig. 3. The shape of the curve appears to be quite similar as the temporal evolution of the Euler characteristic shown in Fig. 6. For sample 4 the number of threefold branching is fluctuating around a more or less constant value [Fig. 10(a)]. For sample 3, however, it increases first slightly and starts to decrease at frame 120. The morphological transition is also visible in the temporal evolution of y connections. When the structure does not change the curve fluctuates around a constant mean. Computing the correlation functions for the two curves [Fig. 10(b)] a similar behavior can be seen as in Fig. 7. As the correlation curve corresponding to sample 3 shows a slow decrease with a time constant of 40–50 frames [Fig. 10(b)] the correlation curve belonging to sample 4 decreases very fast indicating that no temporal correlations exist on the studied time scale.

IV. SUMMARY

We have demonstrated and compared three different approaches for quantifying the temporal evolution of the local morphology of the microdomain structure of a thin film of block copolymer. Compared to other methods in the literature [14,16,42,43] local Minkowski functionals and statistics

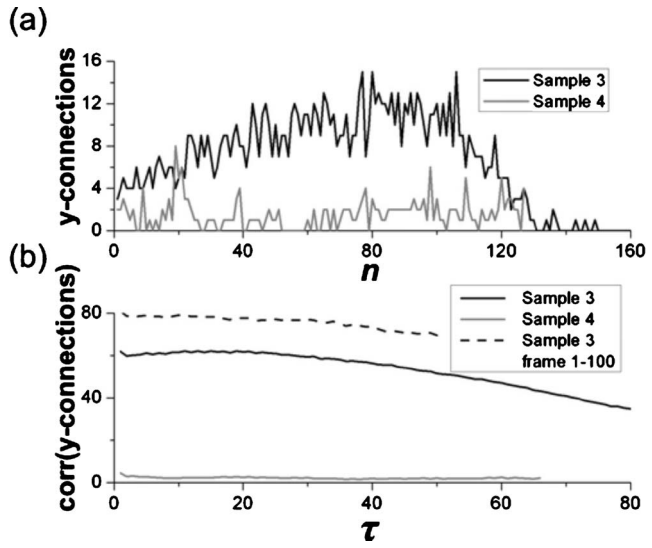

FIG. 10. (a) Number of y connections versus frame number n of samples 3 and 4 corresponding to the data sets shown in Fig. 4(a) and Fig. 4(b), respectively. (b) Correlation function of the number of y connections versus time lag τ. Sample 3 and 4 correspond to the data sets shown in Fig. 4(a) and Fig. 4(b), respectively. For sample 3, also the correlation function for frame 1 to frame 100 is shown. All quantities are dimensionless.

based on the skeletonization of SPM gray scale images have the advantage of analyzing the data in real space. In addition they do not depend on periodic patterns or statistical assumptions. Therefore, they are especially suited for morphologies containing a lot of defects whose evolution should be tracked and whose temporal and lateral correlations should be investigated. Furthermore, Minkowski functionals computed as function of the threshold value require no *a priori* model of the structure. However, these curves contain redundant information. Reducing them to characteristic values which can be tracked over time must be done carefully. We have shown that an interval of thresholds can be identified where different morphologies can be distinguished in a robust way, which does not depend on the particular choice of the threshold value.

Our results show that Minkowski functionals are not only applicable to the analysis of data of structural transitions in block copolymer microdomains [46] but as well to the analysis of the more noisy data in SPM experiments. We analyzed the fluctuations of the time-dependent Euler characteristic and the temporal evolution of y connections by correlation analysis. In both, no characteristic time constants could be detected in the fluctuations. On larger time scales the correlation functions are dominated by structural transitions of the examined patterns. None of the three methods shows a temporal correlation in the microdomain dynamics of the studied data set. The presented methods appear as well suited tools for the search for possible lateral correlations of defect dynamics, which is a topic of future work.

ACKNOWLEDGMENTS

This work was supported by the VolkswagenStiftung and the European Commission (FORCETOOL, Contract No. NMP4-CT-2004-013684). Furthermore, the authors would like to thank Christian Franke for implementing the local Minkowski algorithm and Marcus Böhme for measuring the analyzed image sequence.

[1] C. Park, J. Yoon, and E. L. Thomas, Polymer **44**, 6725 (2003).
[2] R. A. Segalman, H. Yokoyama, and E. J. Kramer, Adv. Mater. **13**, 1152 (2001).
[3] T. L. Morkved, M. Lu, A. M. Urbas, E. E. Ehrichs, H. M. Jaeger, P. Mansky, and T. P. Russell, Science **273**, 931 (1996).
[4] T. Thurn-Albrecht, J. DeRouchey, T. P. Russell, and R. Kolb, Macromolecules **35**, 8106 (2002).
[5] J.-Y. Wang, T. Xu, J. M. Leiston-Belanger, S. Gupta, and T. P. Russell, Phys. Rev. Lett. **96**, 128301 (2006).
[6] D. Angelescu, J. H. Waller, D. H. Adamson, P. Deshpande, S. Y. Chou, R. A. Register, and P. M. Chaikin, Adv. Mater. **16**, 1736 (2004).
[7] D. A. Hajduk, S. M. Gruner, P. Rangarajan, R. A. Register, L. J. Fetters, C. Honeker, R. J. Albalak, and E. L. Thomas, Macromolecules **27**, 490 (1994).
[8] S. Sakurai, T. Hashimoto, and L. J. Fetters, Macromolecules **29**, 740 (1996).
[9] K. Kimishima, T. Koga, and T. Hashimoto, Macromolecules **33**, 968 (2000).
[10] M. W. Matsen, J. Chem. Phys. **114**, 8165 (2001).
[11] A. Knoll, A. Horvat, K. S. Lyakhova, G. Krausch, G. J. A. Sevink, A. V. Zvelindovsky, and R. Magerle, Phys. Rev. Lett. **89**, 035501 (2002).
[12] C.-Y. Wang and T. P. Lodge, Macromolecules **35**, 6997 (2002).
[13] J. Hahm, W. A. Lopes, H. M. Jaeger, and S. J. Sibener, J. Chem. Phys. **109**, 10111 (1998).
[14] C. K. Harrison, D. H. Adamson, Z. Cheng, J. M. Sebastian, S. Sethuraman, D. A. Huse, R. A. Register, and P. M. Chaikin, Science **290**, 1558 (2000).
[15] J. Hahm and S. J. Siebener, J. Chem. Phys. **114**, 4730 (2001).
[16] C. K. Harrison, Z. Cheng, S. Sethuraman, D. A. Huse, P. M. Chaikin, D. A. Vega, J. M. Sebastian, R. A. Register, and D. H. Adamson, Phys. Rev. E **66**, 011706 (2002).
[17] A. Knoll, K. S. Lyakhova, A. Horvat, G. Krausch, G. J. A. Sevink, A. V. Zvelindovsky, and R. Magerle, Nat. Mater. **3**, 886 (2004).
[18] L. Tsarkova, A. Knoll, and R. Magerle, Nano Lett. **6**, 1574 (2006).
[19] L. Tsarkova, A. Horvat, G. Krausch, A. V. Zvelindovsky, G. J. A. Sevink, and R. Magerle, Langmuir **22**, 8089 (2006).
[20] K. Amundson, E. Helfand, D. D. Davis, X. Quan, S. S. Patel, and S. D. Smith, Macromolecules **24**, 6546 (1991).
[21] T. Thurn-Albrecht, J. DeRouchy, T. P. Russell, and H. M. Jäger, Macromolecules **33**, 3250 (2000).
[22] A. Böker, A. Knoll, H. Elbs, V. Abetz, A. H. E. Müller, and G. Krausch, Macromolecules **35**, 1319 (2002).
[23] A. V. Kyrylyuk, A. V. Zvelindovsky, G. J. A. Sevink, and J. G. E. M. Fraaije, Macromolecules **35**, 1473 (2002); A. V. Zvelindovsky and G. J. A. Sevink, Phys. Rev. Lett. **90**, 049601

(2003).
[24] T. Xu, A. V. Zvelindovsky, G. J. A. Sevink, O. Gang, B. Ocko, Y. Zhu, S. P. Gido, and T. P. Russell, Macromolecules **37**, 6980 (2004).
[25] T. Xu, A. V. Zvelindovsky, G. J. A. Sevink, K. S. Lyakhova, H. Jinnai, and T. P. Russell, Macromolecules **38**, 10788 (2005).
[26] K. Schmidt, A. Böker, H. Zettl, F. Schubert, H. Hänsel, F. Fischer, T. M. Weiss, V. Abetz, A. V. Zvelindovsky, G. J. A. Sevink, and G. Krausch, Langmuir **21**, 11974 (2005).
[27] V. Olszowka, M. Hund, V. Kuntermann, S. Scherdel, L. Tsarkova, A. Böker, and G. Krausch, Soft Matter **2**, 1089 (2006).
[28] K. Schmidt, H. G. Schoberth, F. Schubert, H. Hänsel, F. Fischer, T. M. Weiss, G. J. A. Sevink, A. V. Zvelindovsky, A. Böker, and G. Krausch, Soft Matter **3**, 448 (2007).
[29] K. I. Winey, S. S. Patel, R. G. Larson, and H. Watanabe, Macromolecules **26**, 4373 (1993).
[30] G. Schmidt, W. Richtering, P. Lindner, and P. Alexandridis, Macromolecules **31**, 2293 (1998).
[31] A. V. Zvelindovsky, G. J. A. Sevink, B. A. C. van Vlimmeren, N. M. Maurits, and J. G. E. M. Fraaije, Phys. Rev. E **57**, R4879 (1998).
[32] A. V. Zvelindovsky, G. J. A. Sevink, and J. G. E. M. Fraaije, Phys. Rev. E **62**, R3063 (2000).
[33] A. V. Zvelindovsky and G. J. A. Sevink, Europhys. Lett. **62**, 370 (2003).
[34] J. Bodycomb, Y. Funaki, K. Kimishima, and T. Hashimoto, Macromolecules **32**, 2075 (1999).
[35] I. W. Hamley, V. Castelletto, O. O. Mykhaylyk, and Z. Yang, Langmuir **20**, 10785 (2004).
[36] G. Binning, H. Rohrer, C. Gerber, and E. Weibel, Phys. Rev. Lett. **49**, 57 (1982).
[37] S. N. Magonov and M.-H. Whangbo, *Surface Analysis with STM and AFM* (VCH, Weinheim, 1996).
[38] P. K. Hansma, G. Schitter, G. E. Fantner, and C. Prater, Science **314**, 601 (2006).
[39] K. S. Lyakhova, A. Horvat, A. V. Zvelindovsky, and G. J. A. Sevink, Langmuir **22**, 5848 (2006).
[40] K. S. Lyakhova, A. V. Zvelindovsky, and G. J. A. Sevink, Macromolecules **39**, 3024 (2006).
[41] S. Scherdel, H. G. Schoberth, and R. Magerle, J. Chem. Phys. **127**, 014903 (2007).
[42] R. A. Segalman, A. Hexemer, R. C. Hayward, and E. J. Kramer, Macromolecules **36**, 3272 (2003).
[43] R. A. Segalman, A. Hexemer, and E. J. Kramer, Macromolecules **36**, 6831 (2003).
[44] D. A. Vega, C. K. Harrison, D. E. Angelescu, M. L. Trawick, D. A. Huse, P. M. Chaikin, and R. A. Register, Phys. Rev. E **71**, 061803 (2005).
[45] P. Soille, *Morphological Image Analysis* (Springer, New York, 2003).
[46] G. J. A. Sevink and A. V. Zvelindovsky, J. Chem. Phys. **121**, 3864 (2004).
[47] M. Pinna, A. V. Zvelindovsky, S. Todd, and G. Goldbeck-Wood, J. Chem. Phys. **125**, 154905 (2006).
[48] G. J. A. Sevink, in *Nanostructured Soft Matter: Experiments, Theory Perspectives*, edited by A. V. Zvelindovsky (Springer, New York, 2007).
[49] A. Rosenfeld and A. C. Kak, *Digital Picture Processing* (Academic, New York, 1976).
[50] J. Serra, *Image Analysis and Mathematical Morphology* (Academic, New York, 1982).
[51] L. A. Santaló, *Integral Geometry and Geometric Probability* (Addison-Wesley, Reading, MA, 1976).
[52] K. R. Mecke, Int. J. Mod. Phys. B **12**, 861 (1998).
[53] K. R. Mecke, *Additivity, Convexity, and Beyond: Applications of Minkowski Functionals in Statistical Physics*, Lecture Notes in Physics (Springer, New York, 2000), Vol. 554, p. 111.
[54] K. R. Mecke, Phys. Rev. E **53**, 4794 (1996).
[55] J. Becker, G. Grün, R. Seemann, H. Mantz, K. Jacobs, K. Mecke, and R. Blossey, Nat. Mater. **2**, 59 (2003); R. Fetzer, M. Rauscher, R. Seemann, K. Jacobs, and K. Mecke, Phys. Rev. Lett. **99**, 114503 (2007).
[56] C. H. Arns, M. A. Knackstedt, W. V. Pinczewski, and K. R. Mecke, Phys. Rev. E **63**, 031112 (2001); C. H. Arns, M. A. Knackstedt, and K. R. Mecke, Phys. Rev. Lett. **91**, 215506 (2003).
[57] K. Jacobs, R. Seemann, and K. Mecke, *Dynamics of Dewetting and Structure Formation in Thin Liquid Films*, Lecture Notes in Physics (Springer, New York, 2000), Vol. 554, p. 72.
[58] K. Michielsen, H. De Raedt, and J. G. E. M. Fraaije, Prog. Theor. Phys. Suppl. **138**, 543 (2000).
[59] A. Aksimentiev, K. Moorthi, and R. Holyst, J. Chem. Phys. **112**, 6049 (2000).
[60] *Morphology of Condensed Matter. Physics and Geometry of Spatially Complex Systems*, edited by K. R. Mecke and D. Stoyan, Lecture Notes in Physics (Springer, New York, 2002), Vol. 600.
[61] J. S. Gutmann, P. Müller-Buschbaum, and M. Stamm, Faraday Discuss. **112**, 285 (1999).
[62] J. Raczkowska, J. Rysz, A. Budkowski, J. Lekki, M. Lekka, A. Bernasik, K. Kowalski, and P. Czuba, Macromolecules **36**, 2419 (2003).
[63] A. Bernasik, J. Rysz, A. Budkowski, R. Brenn, K. Kowalski, J. Camra, and J. Jedliński, Eur. Phys. J. E **12**, 211 (2003).
[64] J. Raczkowska, A. Bernasik, A. Budkowski, K. Sajewicz, B. Penc, J. Lekki, M. Lekka, J. Rysz, K. Kowalski, and P. Czuba, Macromolecules **37**, 7308 (2004).
[65] J. Raczkowska, A. Bernasik, A. Budkowski, J. Rysz, K. Kowalski, M. Lekka, P. Czuba, and J. Lekki, Thin Solid Films **476**, 358 (2005).
[66] J. Raczkowska, P. Cyganik, A. Budkowski, A. Bernasik, J. Rysz, I. Raptis, P. Czuba, and K. Kowalski, Macromolecules **38**, 8486 (2005).
[67] J. Raczkowska, A. Bernasik, A. Budkowski, P. Cyganik, J. Rysz, I. Raptis, and P. Czuba, Surf. Sci. **600**, 1004 (2006).
[68] M. Böhme, thesis, Technische Universität Chemnitz, 2007.
[69] A. Knoll, R. Magerle, and G. Krausch, J. Chem. Phys. **120**, 1105 (2004).
[70] NanoScope Software 6.13, Veeco Instuments Inc.
[71] S. Scherdel, S. Wirtz, N. Rehse, and R. Magerle, Nanotechnology **17**, 881 (2006).
[72] H. Hadwiger, *Vorlesungen über Inhalt, Oberfläche und Isoperimetrie* (Springer, Berlin, 1957).
[73] L. Lam, S.-W. Lee, and C. Y. Suen, IEEE Trans. Pattern Anal. Mach. Intell. **14**, 869 (1992).
[74] M. W. Jones, J. A. Bærentzen, and M. Sramek, IEEE Trans. Vis. Comput. Graph. **12**, 581 (2006).
[75] See also Ref. [45], p. 340.
[76] K. Mecke and D. Stoyan, Biom. J. **47**, 473 (2005).